

Cite this: *Phys. Chem. Chem. Phys.*, 2012, **14**, 9323–9329

www.rsc.org/pccp

PAPER

Probing the electronic structure and chemical bonding of the “staple” motifs of thiolate gold nanoparticles: $\text{Au}(\text{SCH}_3)_2^-$ and $\text{Au}_2(\text{SCH}_3)_3^-$ †

Chuan-Gang Ning,^{‡a} Xiao-Gen Xiong,^b Yi-Lei Wang,^b Jun Li^{*b} and Lai-Sheng Wang^{*a}

Received 6th November 2011, Accepted 9th December 2011

DOI: 10.1039/c2cp23490d

Thiolate-protected gold nanoparticles have been found recently to be coordinated by the so-called “staple” bonding motifs, consisting of quasi-linear [RS–Au–SR] and V-shaped [RS–Au–(SR)–Au–SR] units, which carry a negative charge formally. Using photoelectron spectroscopy (PES) in conjunction with *ab initio* calculations, we have investigated the electronic structure and chemical bonding of the simplest staples with $\text{R} = \text{CH}_3$: $\text{Au}(\text{SCH}_3)_2^-$ and $\text{Au}_2(\text{SCH}_3)_3^-$, which were produced by electrospray ionization. PES data of the two Au–thiolate complexes are obtained both at room temperature (RT) and 20 K. The temperature-dependent study reveals significant spectral broadening at RT, in agreement with theoretical predictions of multiple conformations due to the different orientations of the $-\text{SCH}_3$ groups. The Au–S bonds in $\text{Au}_n(\text{SCH}_3)_{n+1}^-$ ($n = 1, 2$) are shown to be covalent *via* a variety of chemical bonding analyses. The strong Au–thiolate bonding and the stability of the Au–thiolate complexes are consistent with their ubiquity as staples for gold nanoparticles and on gold surfaces.

1. Introduction

The thiolate ligand (RS–, $\text{R} =$ organic group) is widely used in self-assembled monolayers (SAMs) on gold surfaces¹ and ligand-protected gold nanoparticles.^{2–6} Knowledge about the Au–S bond and the detailed atomic structures of the thiolate–substrate interface is critical to understand the electronic, optical, chemical, and structural properties of SAMs and gold nanoparticles. However, the interfacial structures of SAMs on gold surfaces were controversial for many years (see ref. 7 and references therein). It was only in 2006 that the gold–adatom-mediated bonding in self-assembled alkanethiolates on Au(111) surface was observed in high resolution STM experiments.⁷ In this bonding mode, instead of a single thiolate adsorbed atop an Au atom on the surface, an adatom is lifted from the surface to form a quasilinear RS–Au–SR unit, which is coordinated to the underlying substrate *via* S–Au and Au–Au interactions. This finding was followed in 2007 by the remarkable crystallization and X-ray structural determination of the first thiolate-protected gold nanoparticles,

$\text{Au}_{102}(\text{p-MBA})_{44}$ ($\text{p-MBA} = \textit{para}$ -mercaptobenzoate or $\text{p-S-C}_6\text{H}_4\text{-COOH}$), which were found to consist of a Au_{79} core coordinated by 19 RS–Au–SR units (identical to those observed on the Au surface⁷) and two RS–Au–SR–Au–SR units.⁸ The discovery of these “staple” bonding motifs in $\text{Au}_{102}(\text{p-MBA})_{44}$ has been a milestone and led to rapid progress in the computational^{9–13} and experimental^{14–24} characterization of well-defined gold nanoparticles, such as the syntheses and characterization of $\text{Au}_{25}(\text{SR})_{18}$,^{14,15} $\text{Au}_{68}(\text{SR})_{34}$,¹⁸ $\text{Au}_{20}(\text{SR})_{16}$,¹⁹ $\text{Au}_{38}(\text{SR})_{24}$,^{23a} $\text{Au}_{19}(\text{SR})_{13}$,^{23b} $\text{Au}_{144}(\text{SR})_{60}$,^{23c} and $\text{Au}_{36}(\text{SR})_{23}$.²⁴ The RS–Au–SR and RS–Au–SR–Au–SR staple motifs can be viewed as carrying a single negative charge, in which the Au atoms are in their +1 oxidation state.

In the current article, we report a study of the electronic structure and chemical bonding of the two simplest staple motifs with $\text{R} = \text{CH}_3$, $\text{Au}(\text{SCH}_3)_2^-$ and $\text{Au}_2(\text{SCH}_3)_3^-$, using anion photoelectron spectroscopy and *ab initio* calculations. We are able to prepare these complexes using electrospray ionization and probe their electronic structure using photoelectron spectroscopy (PES) both at room temperature (RT) and 20 K. The photoelectron spectra at low temperature show significant differences from those at RT. Theoretical calculations based on density functional theory (DFT) and *ab initio* wave function theory (WFT) have been carried out to aid interpretation of the spectra and chemical bonding analyses. It is found that the strong temperature-dependent spectra arise from coexistence of multiple conformers of $\text{Au}_n(\text{SCH}_3)_{n+1}^-$ ($n = 1, 2$). The Au–S bond is analyzed using a number of different methods and is found to exhibit significant covalency.

^a Department of Chemistry, Brown University, Providence, Rhode Island 02912, USA. E-mail: Lai-Sheng_Wang@brown.edu

^b Department of Chemistry & Key Laboratory of Organic Optoelectronics and Molecular Engineering of Ministry of Education, Tsinghua University, Beijing 100084, China. E-mail: junli@mail.tsinghua.edu.cn

† This paper is dedicated to Prof. Dr Ludger Wöste on the occasion of his 65th birthday.

‡ Current address: Department of Physics, Tsinghua University, Beijing 100084, China.

2. Experimental and theoretical methods

2.1. Photoelectron spectroscopy

The experiments at RT were carried out using a magnetic-bottle PES apparatus equipped with an ESI source.²⁵ The low temperature PES experiments were conducted on our second-generation ESI-PES apparatus, equipped with a cryogenically controlled ion trap.²⁶ In the current experiment, the ion trap was operated at 20 K. The $\text{Au}_n(\text{SCH}_3)_{n+1}^-$ ($n = 1, 2$) anion species were produced *via* electrospray of a 0.1 mM solution of sodium methyl thiolate (NaSCH_3) and chloro(triphenylphosphine)gold(I) (AuClPPh_3) (mass ratio $\sim 1:1$) in dimethylformamide (DMF) solvent. With this solution, we could also observe $\text{Au}_3(\text{SCH}_3)_4^-$, but its mass intensity was too weak for further PES experiment. It is interesting to note that we readily observed a strong Au^- signal under the current ESI conditions, providing a convenient PES calibrant along with I^- and Br^- anions.

The desired anions were selected and decelerated before being detached by a laser beam in the interaction zone of a magnetic-bottle photoelectron analyzer. The 193 nm (6.424 eV) radiation from an ArF excimer laser and 266 nm (4.661 eV) light from a Nd:YAG laser were used in the present work. The detachment lasers were run at a 20 Hz repetition rate, while the ion trap was operated at 10 Hz. The ion beam was off at alternating detachment laser shots for background subtraction. Photoelectron spectra of Au^- , I^- , and Br^- were used for calibration. Typical energy resolution of our two ESI-PES apparatuses was 2%, *i.e.*, 20 meV for 1 eV photoelectrons.^{25,26}

2.2. Computational details

The theoretical calculations were performed using relativistic DFT methods and *ab initio* coupled-cluster methods. The DFT calculations were done using the generalized gradient approximations (GGA) with the PBE exchange-correlation functional²⁷ implemented in the Amsterdam Density Functional (ADF2009.1) program.²⁸ The uncontracted Slater basis sets with the quality of triple- ζ plus two polarization functions (TZ2P) were used for all the elements, with the frozen core approximation applied to $[1s^2-4f^4]$ for Au, $[1s^2]$ for C, and $[1s^2-2p^6]$ for S.²⁸ The scalar relativistic (SR) and spin-orbit (SO) coupling effects were taken into account by the zero-order-regular approximation (ZORA).²⁹ Geometries were optimized at the PBE SR-ZORA level and single-point energy calculations were carried out with inclusion of the SO effects. Vibrational frequency calculations were carried out to verify if the obtained structures were true minima or transition states. Because gold complexes are known to exhibit complicated electron correlations (including dispersion effects), high-level CCSD(T)³⁰ single-point energy calculations were performed using the MOLPRO2008 program,³¹ at the PBE geometries from Gaussian03.³² In the MOLPRO and Gaussian03 calculations, the cc-pVTZ-PP basis set optimized for the energy-consistent pseudo-potential ECP60MDF³³ was used for Au, and the aug-cc-pVTZ basis sets were used for S, C, and H.³⁴ To further understand the nature of the chemical bonding between Au–S, a variety of theoretical tools were applied. Natural resonance theory (NRT)³⁵ calculations were performed using NBO5.0.³⁶ Electron localization function (ELF)³⁷ calculations with all-electron basis sets were done by the DENSF utility in ADF2009.1.

3. Experimental results

3.1. Photoelectron spectra of $\text{Au}(\text{SCH}_3)_2^-$ and their strong temperature dependence

Fig. 1a shows the 266 nm photoelectron spectra of $\text{Au}(\text{SCH}_3)_2^-$ obtained at RT (black curve) and 20 K (red curve). The first two features X and A are very broad, especially at RT. In contrast, peak B is much sharper and is vibrationally resolved at 20 K, as shown more clearly in Fig. 1b. The adiabatic detachment energy (ADE) was determined as 3.33 ± 0.03 eV using the onset of feature X at 20 K, which also represents the electron affinity of neutral $\text{Au}(\text{SCH}_3)_2$. Because the X band was not vibrationally resolved, the ADE was obtained by drawing a straight line along the leading edge of the X band in the 20 K spectrum and then adding the instrumental resolution to the intersection with the binding energy axis. The first vertical detachment energy (VDE1) was measured as 3.47 eV from the maximum of band X. At 20 K, there are resolvable vibrational structures in band B, which are expanded in Fig. 1b. To more accurately determine the vibrational spacings, we fitted the vibrational peaks in Fig. 1b by Gaussians. There are two observable vibrational progressions in band B: their vibrational frequencies were determined as 170 ± 40 cm^{-1} for the low frequency mode and 725 ± 40 cm^{-1} for the higher frequency mode. At 193 nm, four additional bands (C–F) were observed, as shown in Fig. 1c. The VDEs of all the observed PES bands are given in Table 1 and compared with theoretical calculations (*vide infra*).

Major differences for bands X and A were observed at RT and 20 K. These two bands became significantly narrower at 20 K (red curves in Fig. 1a and c). The threshold binding energy of band X increased by about 0.3 eV in the 20 K spectra relative to

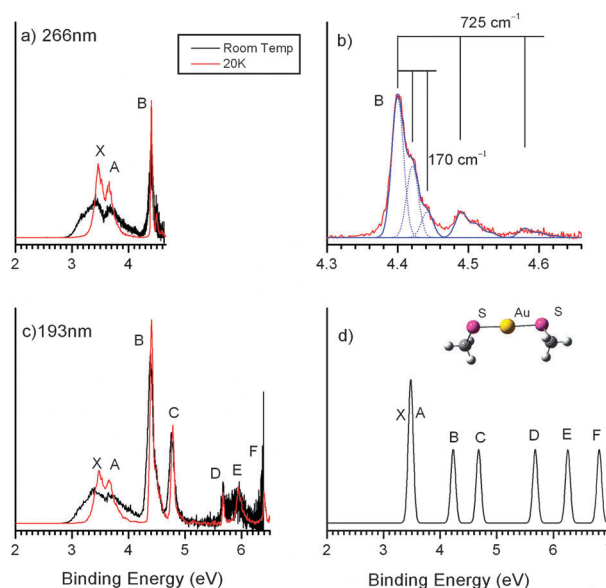


Fig. 1 Photoelectron spectra of $\text{Au}(\text{SCH}_3)_2^-$ compared with the simulated spectrum. (a) The 266 nm spectra at room temperature (black curve) and 20 K (red curve). (b) Expansion of band B of the 20 K spectrum at 266 nm, showing details of the resolved vibrational structures. The blue curves are Gaussian fittings. (c) The 193 nm spectra at room temperature (black curve) and 20 K (red curve). (d) Simulated spectrum of the C_2 ground state of $\text{Au}(\text{SCH}_3)_2^-$. The optimized structure is shown in the inset. See Table 2 for structural details.

Table 1 Observed and calculated vertical detachment energies (VDEs) for $\text{Au}(\text{SCH}_3)_2^-$, and the relevant molecular orbital (MO) assignments

Observed bands	MO	VDE/eV	
		Exp	Theo
X	11b	3.47	3.51 ^a
A	12a	3.66	3.53
B	10b	4.41	4.27
C	11a	4.79	4.73
D	10a	5.68	5.68
E	9b	5.94	6.26
F	9a	6.40	6.81

^a VDE(1) is calculated using CCSD(T) and corrected with the SO coupling values from PBE/TZ2P calculations, and VDEs for orbitals 12a, 10b, 11a are calculated using the scalar relativistic (SR) CCSD(T). The other VDEs for orbitals 10a, 9b, 9a are calculated using the GKT approximation (see text and ref. 38).

those at RT (black curves in Fig. 1a and c). In contrast, bands B–F are all relatively sharp and well separated and they do not exhibit the dramatic temperature dependence as bands X and A: there is only minor thermal broadening at RT compared with those at 20 K, as expected. The strong temperature dependence of bands X and A may suggest the presence of isomers or conformers at RT for $\text{Au}(\text{SCH}_3)_2^-$.

3.2. Photoelectron spectra of $\text{Au}_2(\text{SCH}_3)_3^-$

Fig. 2a and b shows the PES spectra of $\text{Au}_2(\text{SCH}_3)_3^-$ at RT (black curve) and 20 K (red curve), and at 266 and 193 nm, respectively. The RT spectra were quite broad and all spectral features were sharpened at 20 K. The electron

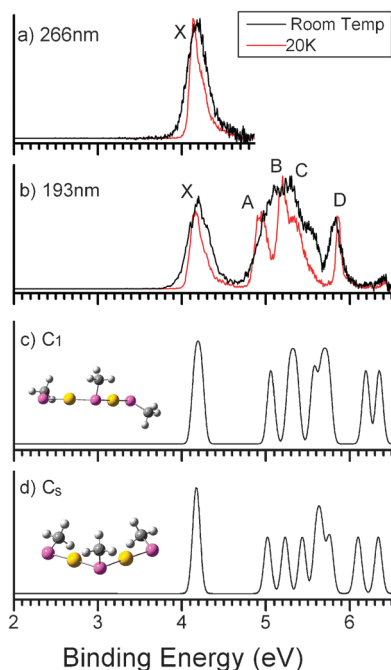


Fig. 2 Photoelectron spectra of $\text{Au}_2(\text{SCH}_3)_3^-$ compared with the simulated spectra. (a) The 266 nm spectra at room temperature (black curve) and 20 K (red curve). (b) The 193 nm spectra at room temperature (black curve) and 20 K (red curve). (c) The simulated spectrum of $\text{Au}_2(\text{SCH}_3)_3^-$ with C_1 symmetry. (d) The simulated spectra of $\text{Au}_2(\text{SCH}_3)_3^-$ with C_s symmetry. The insets in (c) and (d) are the two optimized structures of $\text{Au}_2(\text{SCH}_3)_3^-$. See Fig. 3 for structural details.

binding energies of $\text{Au}_2(\text{SCH}_3)_3^-$ were much higher than those of $\text{Au}(\text{SCH}_3)_2^-$. The 266 nm spectra (Fig. 2a) revealed one spectral band (X). The ADE was determined as 4.06 ± 0.03 eV from the relatively sharp onset of the X band at 20 K. The VDE of band X was measured as 4.14 eV. At 193 nm, four more bands were resolved in the 20 K spectrum with VDEs of 4.9, 5.2, 5.4, and 5.9 eV for bands A, B, C, and D, respectively. Again, we observed significant differences in the PES spectra of $\text{Au}_2(\text{SCH}_3)_3^-$ between RT and 20 K, suggesting the possible presence of low-lying isomers or different conformers at RT, similar to the case of $\text{Au}(\text{SCH}_3)_2^-$.

4. Theoretical results and comparison with experiment

4.1. $\text{Au}(\text{SCH}_3)_2^-$

We calculated various possible structures of $\text{Au}_n(\text{SCH}_3)_{n+1}^-$ ($n = 1, 2$). The methods used and theoretical details are given in Section 2.2. Geometry optimizations showed that the most stable conformer of $\text{Au}(\text{SCH}_3)_2^-$ has C_2 symmetry with a 1A ground state (Table 2). Two rotamers of $\text{Au}(\text{SCH}_3)_2^-$ with C_{2h} and C_{2v} symmetries have slightly higher energies both about 6.8 kJ mol^{-1} above the C_2 ground state and they are both transition states for rotations along the S–Au–S axis. If the entropic effects are considered, the free energies at RT for the two transition states are 10.4 kJ mol^{-1} and 10.0 kJ mol^{-1} above the C_2 state, respectively. However, on the neutral potential energy surface, the C_2 structure is no longer a minimum. There are two local minima for neutral $\text{Au}(\text{SCH}_3)_2$: one is 2B_g with C_{2h} symmetry, and the other is 2A_2 with C_{2v} symmetry (Table 2). The energy difference between the two structures is 0.8 kJ mol^{-1} , and the C_{2h} structure is slightly more stable at the PBE/TZ2P level. If the internal rotation of the methyl group ($-\text{CH}_3$) is further considered, there will be many different conformers that are close in energy for the anion and can coexist in the gas phase, especially at room temperature.

We performed high level CCSD(T) calculations for the first VDE (VDE1) from the ground state C_2 structure. With the spin–orbit corrections from the PBE calculations, the theoretical VDE1 is 3.51 eV at the CCSD(T) level, which is in excellent agreement with the experimental value 3.47 eV (Table 1). The simulated PES spectrum is shown in Fig. 1d, where the binding energies for the first four detachment transitions (X, A, B, C) were obtained *via* CCSD(T) calculations. The binding energies for the higher energy detachment channels (D, E, F) were calculated using the generalized Koopmans's theorem (GKT) by aligning the detachment channel D (10a orbital in Fig. 4) with the experimental peak D.³⁸ The orbital energies were obtained through ADF/PBE/TZ2P calculations at the SO-ZORA level. The calculated VDEs at CCSD(T) for the second, third, and fourth detachment channels are all in excellent agreement with the experimental values (Table 1). The simulated spectral pattern (Fig. 1d) is in good accord with the experimental spectra.

4.2. $\text{Au}_2(\text{SCH}_3)_3^-$

The geometry optimizations indicate that there are two minima for $\text{Au}_2(\text{SCH}_3)_3^-$ with C_s ($^1A'$) and C_1 (1A) symmetries,

Table 2 Structures and relative energies (ΔE) of $\text{Au}(\text{SCH}_3)_2^-$ and its neutral form (in parentheses) calculated at the PBE/TZ2P level^a

	C_2	C_{2h}	C_{2v}
$R(\text{Au-S})/\text{\AA}$	2.321	2.336 (2.266)	2.336 (2.266)
$\angle \text{Au-S-C} (^{\circ})$	104.15	104.14	104.19
$\angle \text{S-Au-S} (^{\circ})$	177.80	180.00 (180.00)	176.51 (175.93)
$d\angle \text{C-S-S-C} (^{\circ})$	93.49	180.00	0.00
$\Delta E/\text{kJ mol}^{-1}$	0.0	6.8 (0.0)	6.8 (0.8)

^a For anions, the C_2 structure is the ground state while the C_{2h} and C_{2v} structures are transition states.

respectively, as shown in Fig. 3. The energy difference between these two conformers is very small, only 1.3 kJ mol^{-1} at the SO-ZORA PBE level. There are also two minima for neutral $\text{Au}_2(\text{SCH}_3)_3$ with C_s (${}^2A'$) and C_1 (2A) symmetries, respectively (Fig. 3). As high level CCSD(T) calculations were too expensive for $\text{Au}_2(\text{SCH}_3)_3^-$, the simulated PES spectra were obtained by simply adding the orbital energies from the ADF/PBE/TZ2P calculations at the SO-ZORA level to the experimental VDE1 value (4.14 eV) and fitting each transition with a Gaussian of 0.1 eV width, as shown in Fig. 2c and d.

The simulated spectra of both conformers can reproduce the gap between bands X and A in the experimental spectra.

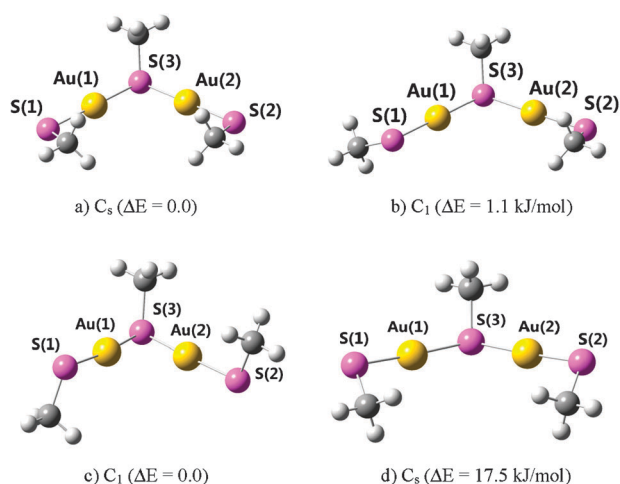


Fig. 3 Optimized structures and relative energies (ΔE) of $\text{Au}_2(\text{SCH}_3)_3^-$ and its neutral form calculated at the PBE/TZ2P level. (a) The C_s ground state of the $\text{Au}_2(\text{SCH}_3)_3^-$ anion: $R_{\text{S1-Au1}} = R_{\text{S2-Au2}} = 2.306 \text{ \AA}$; $R_{\text{S3-Au1}} = R_{\text{S3-Au2}} = 2.335 \text{ \AA}$; $\angle \text{S1-Au1-S3} = \angle \text{S2-Au2-S3} = 177.64^{\circ}$; $\angle \text{Au1-S3-Au2} = 98.37^{\circ}$. (b) The C_1 low-lying isomer of the $\text{Au}_2(\text{SCH}_3)_3^-$ anion: $R_{\text{S1-Au1}} = 2.307 \text{ \AA}$; $R_{\text{S2-Au2}} = 2.306 \text{ \AA}$; $R_{\text{S3-Au1}} = R_{\text{S3-Au2}} = 2.333 \text{ \AA}$; $\angle \text{S1-Au1-S3} = 179.35^{\circ}$; $\angle \text{S2-Au2-S3} = 176.26^{\circ}$; $\angle \text{Au1-S3-Au2} = 105.85^{\circ}$. (c) The C_1 ground state of the $\text{Au}_2(\text{SCH}_3)_3$ neutral: $R_{\text{S1-Au1}} = 2.272 \text{ \AA}$; $R_{\text{S2-Au2}} = 2.271 \text{ \AA}$; $R_{\text{S3-Au1}} = R_{\text{S3-Au2}} = 2.353 \text{ \AA}$; $\angle \text{S1-Au1-S3} = 171.19^{\circ}$; $\angle \text{S2-Au2-S3} = 170.53^{\circ}$; $\angle \text{Au1-S3-Au2} = 75.14^{\circ}$. (d) The C_s low-lying isomer of the $\text{Au}_2(\text{SCH}_3)_3$ neutral: $R_{\text{S1-Au1}} = R_{\text{S2-Au2}} = 2.277 \text{ \AA}$; $R_{\text{S3-Au1}} = R_{\text{S3-Au2}} = 2.310 \text{ \AA}$; $\angle \text{S1-Au1-S3} = \angle \text{S2-Au2-S3} = 176.98^{\circ}$; $\angle \text{Au1-S3-Au2} = 109.46^{\circ}$.

However, the agreement between the simulation and the experiment for the higher binding energy transitions can only be considered to be qualitative (Fig. 2). Because of the small energy difference between the C_s ${}^1A'$ and C_1 1A structures, the RT spectra for $\text{Au}_2(\text{SCH}_3)_3^-$ most likely contain contributions from both conformers (Fig. 3). The sharpening of the PES spectra at 20 K is probably due to the reduction of the population of the C_1 isomer in the ion beam.

5. Discussions

5.1. The PES spectra of $\text{Au}(\text{SCH}_3)_2^-$ and their temperature dependence

The remarkable temperature dependence of the PES spectra of $\text{Au}(\text{SCH}_3)_2^-$ (Fig. 1) suggests the co-existence of multiple conformers at RT. This observation is supported by the theoretical calculations, considering the flexibility of the backbone of $\text{Au}(\text{SCH}_3)_2^-$, in particular, the rotation along the Au-S and S-C bonds (Table 2). Our calculations showed that the two C_{2v} and C_{2h} transition states of $\text{Au}(\text{SCH}_3)_2^-$ are not too high in energy relative to the C_2 ground state and may be accessible at RT. To check the conformational influence on the PES spectra, we simulated the PES spectra of the C_{2v} and C_{2h} conformers and found that the major difference on comparison with that of the C_2 ground state was in the positions of the first two peaks. The first two detachment channels correspond to electron removal from molecular orbitals that involve weak antibonding interactions between S $3p_x$ or $3p_y$ orbitals and Au $5d$ orbitals, as shown in Fig. 4. When the dihedral angle of C-S-S-C is changed, the overlaps between the atomic orbitals of S and Au will be altered, leading to variation of the molecular orbital energies of HOMO (11b) and HOMO - 1 (12a). The higher binding energy peaks (B-F) come from electron detachment from primarily nonbonding S $3p_z$ orbital (10b) and Au $5d$ orbitals (11a, 10a, 9b, 9a), as shown in Fig. 4. The dihedral angle change has relatively little effect on the energies of these molecular orbitals. Therefore, the higher binding energy bands (B-F) display relatively weak temperature dependence, even though different conformations are populated at RT.

The large geometry change between the anion ground state and the neutral states also contributes to the observed spectral

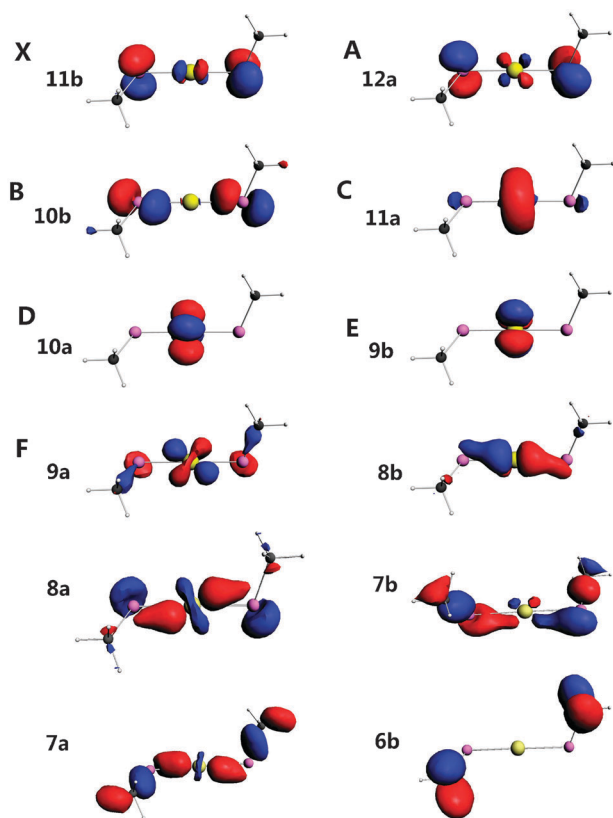


Fig. 4 Kohn-Sham molecular orbitals of $\text{Au}(\text{SCH}_3)_2^-$ (isocontour = 0.06 atomic unit). The labels X, (A–D) indicate the orbital assignments, corresponding to the related experimental features (see Fig. 1).

widths. Detachment from the HOMO of $\text{Au}(\text{SCH}_3)_2^-$ will lead to the C_{2v} neutral state. The neutral state is even more fluxional along the rotation of the Au–S bonds from the fact that the C_{2v} and C_{2h} local minima are almost degenerate (Table 2). The B band, derived from electron detachment of the nonbonding S $3p_z$ orbital (10b in Fig. 4), corresponds to an excited state of neutral $\text{Au}(\text{SCH}_3)_2$ and its vibrational frequencies cannot be directly computed. Based on the calculated vibrational frequencies for the anion ground state at the PBE level, the 170 cm^{-1} mode is assigned to the swing of $-\text{SCH}_3$ ligand, and the 725 cm^{-1} mode is related to the S–C stretching mode.

5.2. Chemical bonding analyses of $\text{Au}(\text{SCH}_3)_2^-$ and $\text{Au}_2(\text{SCH}_3)_3^-$

The isosurfaces of the calculated Kohn-Sham molecular orbitals shown in Fig. 4 reveal strong orbital overlaps between Au and S (7a, 7b, 8a, and 8b orbitals), indicating significant Au–S covalent bonding. Natural resonance theory (NRT) and electron localization function (ELF) calculations have been carried out to provide further insight into the nature of the Au–S bonding. Several other types of charge population and bonding analyses were also performed, as shown in Table 3. NRT is a theoretical method based on quantum chemical calculations to describe molecules with significant resonance structures in terms of classic valence-bond concepts. Our calculations using NRT show that the bond order between Au and S is about 0.49. We found that the ionic and covalent

Table 3 Atomic net charges and bond orders for the C_2 ground state of $\text{Au}(\text{SCH}_3)_2^-$

Charge population							
	NPA ⁴⁷	Hirshfeld ⁴⁸	Voronoi ⁴⁹	MDC-q ⁵⁰	AIM ⁵¹		
Au	0.18	−0.10	−0.08	−0.17	−0.07		
S	−0.42	−0.32	−0.37	−0.36	−0.37		
Bond orders							
	Mayer ⁵²	G-J ⁵³	N-M(3) ⁵⁴	Wiberg ⁵⁵	NAO ^{a, 36}	NPA ^{a, 47}	NRT ³⁵
Au–S	0.89	0.58	0.77	0.55	0.48	0.35	0.49

^a The 3-center-4-electron hyperbond search was used.

contributions to the Au–S bond are almost equal with 0.26 and 0.23, respectively. The charge population analyses and bond orders from other methods (Table 3) are largely consistent with the NRT analyses. Note that the NPA method gives a slight positive charge on Au, while all other methods give a slight negative charge on Au. We have carried out similar bonding analyses for the two structures of $\text{Au}_2(\text{SCH}_3)_3^-$ and found that the Au–S bonding in the larger complex is similar to that in $\text{Au}(\text{SCH}_3)_2^-$.

Electron localization function (ELF) is a chemically intuitive tool to estimate the probability of finding electron pairs in space, and an ELF analysis can show the difference among covalent bonds, ionic bonds, and lone pairs.³⁷ As shown in Fig. 5, significant covalence in the Au–S bonds in $\text{Au}(\text{SCH}_3)_2^-$ and $\text{Au}_2(\text{SCH}_3)_3^-$ is revealed from the ELF analyses. The partial covalent nature of the Au–S bond is important for understanding the unique properties of thiolate-capped gold

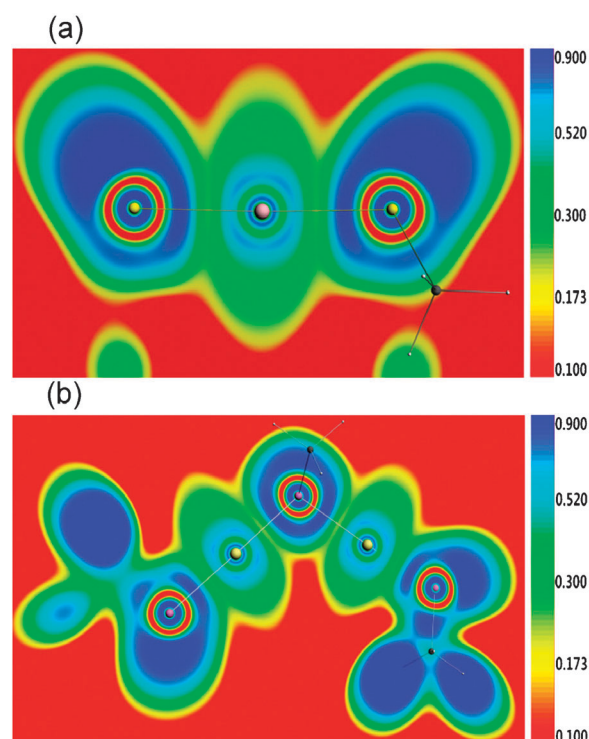


Fig. 5 The electron localization function (ELF) for (a) the C_2 $\text{Au}(\text{SCH}_3)_2^-$ and (b) the C_s $\text{Au}_2(\text{SCH}_3)_3^-$ ground states calculated with the PBE functional.

nanoparticles. Thiolate ligands are known to be the best and most popular ligands for the synthesis of gold nanoparticles. The significant Au–S covalent interactions provide chemical and thermodynamic stability for the thiolate-protected gold nanoparticles. The propensity for covalent bonding by Au has been found in many gold-containing species,³⁹ such as Au(CN)₂[−],⁴⁰ AuO₂[−]/AuS₂[−],⁴¹ AuI₂[−],⁴² and Au₂(CO)₂[−].⁴³ The Au–S covalent interactions have been shown in cyclic thiolated gold clusters from previous DFT calculations.⁴⁴ The unique Au–S covalent bond, in contrast to the largely ionic Ag–S or Cu–S bonds, is mainly ascribed to the maximum relativistic effects for gold among elements with $Z \leq 100$, which leads to significant s–d hybridization for Au (5d¹⁰6s¹).^{45,46}

6. Conclusions

The electronic structures and chemical bonding of the two staple motifs Au(SCH₃)₂[−] and Au₂(SCH₃)₃[−], which cap thiolate-protected gold nanoparticles, are investigated by temperature-dependent photoelectron spectroscopy and theoretical calculations. The remarkable difference between the photoelectron spectra of Au(SCH₃)₂[−] at room temperature and at 20 K is due to the coexistence of multiple conformers. Chemical bonding analyses using a variety of theoretical methods reveal that the Au–S bonds in the thiolate–gold staple motifs contain significant covalent contributions. This covalency plays an important role for the gold–sulfur interactions in gold–thiol nanoparticles.

Acknowledgements

We thank Dr Jie Yang and Dr Xue-Bin Wang for help with the initial experiment. The experimental work was supported by the U. S. National Science Foundation (CHE-1049717). The theoretical work was supported by NKBRFSF (2011CB932400) and NSFC (20933003, 11079006, 91026003) of China. The calculations were performed using the DeepComp 7000 computer at the Supercomputer Center of the Computer Network Information Center, Chinese Academy of Sciences and the Shanghai Supercomputing Center.

References

- C. D. Bain and G. M. Whitesides, *Angew. Chem., Int. Ed. Engl.*, 1989, **28**, 506–512.
- M. Brust, M. Walker, D. Bethell, D. J. Schiffrin and R. Whyman, *Chem. Commun.*, 1994, 801–802.
- R. L. Whetten, J. T. Khoury, M. M. Alvarez, S. Murthy, I. Vezmar, Z. L. Wang, P. W. Stephens, C. L. Cleveland, W. D. Luedtke and U. Landman, *Adv. Mater.*, 1996, **8**, 428–433.
- A. C. Templeton, M. P. Wuefling and R. W. Murray, *Acc. Chem. Res.*, 2000, **33**, 27–36.
- R. Jin, *Nanoscale*, 2010, **2**, 343–362.
- R. Jin, Y. Zhu and H. Qian, *Chem.–Eur. J.*, 2011, **17**, 6584–6593.
- P. Maksymovych, D. C. Sorescu and J. T. Yates, *Phys. Rev. Lett.*, 2006, **97**, 146103.
- P. D. Jadzinsky, G. Calero, C. J. Ackerson, D. A. Bushnell and R. D. Kornberg, *Science*, 2007, **318**, 430–433.
- M. Walter, J. Akola, O. Lopez-Acevedo, P. D. Jadzinsky, G. Calero, C. J. Ackerson, R. L. Whetten, H. Gronbeck and H. Hakkinen, *Proc. Natl. Acad. Sci. U. S. A.*, 2008, **105**, 9157–9162.
- J. Akola, M. Walter, R. L. Whetten, H. Hakkinen and H. Gronbeck, *J. Am. Chem. Soc.*, 2008, **130**, 3756–3757.

- (a) Y. Pei, Y. Gao and X. C. Zeng, *J. Am. Chem. Soc.*, 2008, **130**, 7830–7832; (b) Y. Pei, Y. Gao, N. Shao and X. C. Zeng, *J. Am. Chem. Soc.*, 2009, **131**, 13619–13621.
- (a) K. A. Kacprzak, O. Lopez-Acevedo, H. Hakkinen and H. Gronbeck, *J. Phys. Chem. C*, 2010, **114**, 13571–13576; (b) O. Lopez-Acevedo, H. Tsunoyama, T. Tsukuda, H. Hakkinen and C. M. Aikens, *J. Am. Chem. Soc.*, 2010, **132**, 8210–8218.
- (a) D. E. Jiang, M. L. Tiago, W. Lou and S. Dai, *J. Am. Chem. Soc.*, 2008, **130**, 2777–2779; (b) D. E. Jiang, R. L. Whetten, W. Lou and S. Dai, *J. Phys. Chem. C*, 2009, **113**, 17291–17295.
- M. W. Heaven, A. Dass, P. S. White, K. M. Holt and R. W. Murray, *J. Am. Chem. Soc.*, 2008, **130**, 3754–3755.
- M. Zhu, C. M. Aikens, F. J. Hollander, G. C. Schatz and R. Jin, *J. Am. Chem. Soc.*, 2008, **130**, 5883–5885.
- N. K. Chaki, Y. Negishi, H. Tsunoyama, Y. Shichibu and T. Tsukuda, *J. Am. Chem. Soc.*, 2008, **130**, 8608–8610.
- H. Qian and R. Jin, *Nano Lett.*, 2009, **9**, 4083–4087.
- A. Dass, *J. Am. Chem. Soc.*, 2009, **131**, 11666–11667.
- M. Zhu, H. Qian and R. Jin, *J. Am. Chem. Soc.*, 2009, **131**, 7220–7221.
- C. A. Fields-Zinna, R. Sardar, C. A. Beasley and R. W. Murray, *J. Am. Chem. Soc.*, 2009, **131**, 16266–16271.
- H. Qian, Y. Zhu and R. Jin, *J. Am. Chem. Soc.*, 2010, **132**, 4583–4585.
- S. Knoppe, A. C. Dharmaratne, E. Schreiner, A. Dass and T. Burgi, *J. Am. Chem. Soc.*, 2010, **132**, 16783–16789.
- (a) H. Qian, W. T. Eckenhoff, Y. Zhu, T. Pintauer and R. Jin, *J. Am. Chem. Soc.*, 2010, **132**, 8280–8281; (b) Z. Wu, M. A. MacDonald, J. Chen, P. Zhang and R. Jin, *J. Am. Chem. Soc.*, 2011, **133**, 9670–9673; (c) H. Qian and R. Jin, *Chem. Mater.*, 2011, **23**, 2209–2217.
- P. R. Nimmala and A. Dass, *J. Am. Chem. Soc.*, 2011, **133**, 9175–9177.
- L. S. Wang, C. F. Ding, X. B. Wang and S. E. Barlow, *Rev. Sci. Instrum.*, 1999, **70**, 1957–1966.
- X. B. Wang and L. S. Wang, *Rev. Sci. Instrum.*, 2008, **79**, 073108.
- J. P. Perdew, K. Burke and M. Ernzerhof, *Phys. Rev. Lett.*, 1996, **77**, 3865–3868.
- ADF 2010.01, SCM, Theoretical Chemistry, Vrije Universiteit, Amsterdam, The Netherlands. G. te Velde, F. M. Bickelhaupt, E. J. Baerends, C. F. Guerra, S. J. A. van Gisbergen, J. G. Snijders and T. Ziegler, *J. Comput. Chem.*, 2001, **22**, 931–967.
- E. van Lenthe, E. J. Baerends and J. G. Snijders, *J. Chem. Phys.*, 1993, **99**, 4597–4610.
- (a) G. D. Purvis and R. J. Bartlett, *J. Chem. Phys.*, 1982, **76**, 1910–1918; (b) G. E. Scuseria, C. L. Janssen and H. F. Schaefer, *J. Chem. Phys.*, 1988, **89**, 7382–7387.
- H. J. Werner, *MOLPRO, Version 2008.1, a package of ab initio programs*, (<http://www.molpro.net>).
- M. J. Frisch, et al., *GAUSSIAN 03 (Revision A.1)*, Gaussian, Inc., Wallingford, CT, 2003.
- K. A. Peterson and C. Pizzarini, *Theor. Chem. Acc.*, 2005, **114**, 283–296.
- K. A. Peterson, B. C. Shepler, D. Figgen and H. Stoll, *J. Phys. Chem. A*, 2006, **110**, 13877–13833.
- (a) E. D. Glendening and F. Weinhold, *J. Comput. Chem.*, 1998, **19**, 593–609; (b) E. D. Glendening, J. K. Badenhoop and F. Weinhold, *J. Comput. Chem.*, 1998, **19**, 628–646.
- J. P. Foster and F. Weinhold, *J. Am. Chem. Soc.*, 1980, **102**, 7211–7218.
- (a) A. D. Becke and K. E. Edgecombe, *J. Chem. Phys.*, 1990, **92**, 5397–5403; (b) A. Savin, J. Flad, H. Preuss, O. Jepsen, O. K. Andersen and H. G. von Schnering, *Angew. Chem.*, 1992, **104**, 186–188.
- The CCSD(T) calculation for Au(SCH₃)₂[−] is very expensive due to the large number of basis sets and the low molecular symmetry. Thus, only vertical detachment energies from the first four orbitals were calculated at this level. The vertical binding energies related to the other orbitals (10a, 9b, and 9a) corresponding to observed bands D, E, and F, respectively, were approximated with the generalized Koopmans's theorem (GKT). See T. Tsuneda, J. W. Song, S. Suzuki and K. Hirao, *J. Chem. Phys.*, 2010, **133**, 174101.
- L. S. Wang, *Phys. Chem. Chem. Phys.*, 2010, **12**, 8694–8705.
- X. B. Wang, Y. L. Wang, J. Yang, X. P. Xing, J. Li and L. S. Wang, *J. Am. Chem. Soc.*, 2009, **131**, 16368–16370.
- H. J. Zhai, C. Bürgel, V. Bonacic-Koutecky and L. S. Wang, *J. Am. Chem. Soc.*, 2008, **130**, 9156–9167.

- 42 Y. L. Wang, X. B. Wang, X. P. Xing, F. Wei, J. Li and L. S. Wang, *J. Phys. Chem. A*, 2010, **114**, 11244–11251.
- 43 Y. L. Wang, H. J. Zhai, L. Xu, J. Li and L. S. Wang, *J. Phys. Chem. A*, 2010, **114**, 1247–1254.
- 44 (a) H. Gronbeck, M. Walter and H. Hakkinen, *J. Am. Chem. Soc.*, 2006, **128**, 10268–10275; (b) B. M. Barngrover and C. M. Aikens, *J. Phys. Chem. A*, 2011, **115**, 11818–11823.
- 45 P. Pyykkö, *Chem. Rev.*, 1988, **88**, 563–594.
- 46 P. Pyykkö, X. G. Xiong and J. Li, *Faraday Discuss.*, 2011, **152**, 169–178.
- 47 A. E. Reed, R. B. Weinstock and F. Weinhold, *J. Chem. Phys.*, 1985, **83**, 735–746.
- 48 (a) F. L. Hirshfeld, *Theor. Chim. Acta*, 1977, **44**, 129–138; (b) K. B. Wiberg and P. R. Rablen, *J. Comput. Chem.*, 1993, **14**, 1504–1508.
- 49 F. M. Bickelhaupt, N. J. R. van Eikema Hommes, C. F. Guerra and E. J. Baerends, *Organometallics*, 1996, **15**, 2923–2931.
- 50 M. Swart, P. T. van Duijnen and J. G. Snijders, *J. Comput. Chem.*, 2001, **22**, 79–88.
- 51 (a) J. I. Rodriguez, A. M. Köster, P. W. Ayers, A. Santos-Valle, A. Vela and G. Merino, *J. Comput. Chem.*, 2009, **30**, 1082–1092; (b) J. I. Rodriguez, R. F. W. Bader, P. W. Ayers, C. Michel, A. W. Gotz and C. Bo, *Chem. Phys. Lett.*, 2009, **472**, 149–152.
- 52 I. Mayer, *Chem. Phys. Lett.*, 1983, **97**, 270–274.
- 53 M. S. Gopinathan and K. Jug, *Theor. Chim. Acta*, 1983, **63**, 497–509.
- 54 A. Michalak, R. L. de Kock and T. Ziegler, *J. Phys. Chem. A*, 2008, **112**, 7256–7263.
- 55 K. A. Wiberg, *Tetrahedron*, 1968, **24**, 1083–1096.